SISTEMAS ESTELARES

Material didáctico para las clases de "Masas *de galaxias*"

Clases teóricas dictadas por:
Dra. Lilia P. Bassino

Comparación de espectros estelares (izq.) con el espectro integrado de una galaxia elíptica (der.)

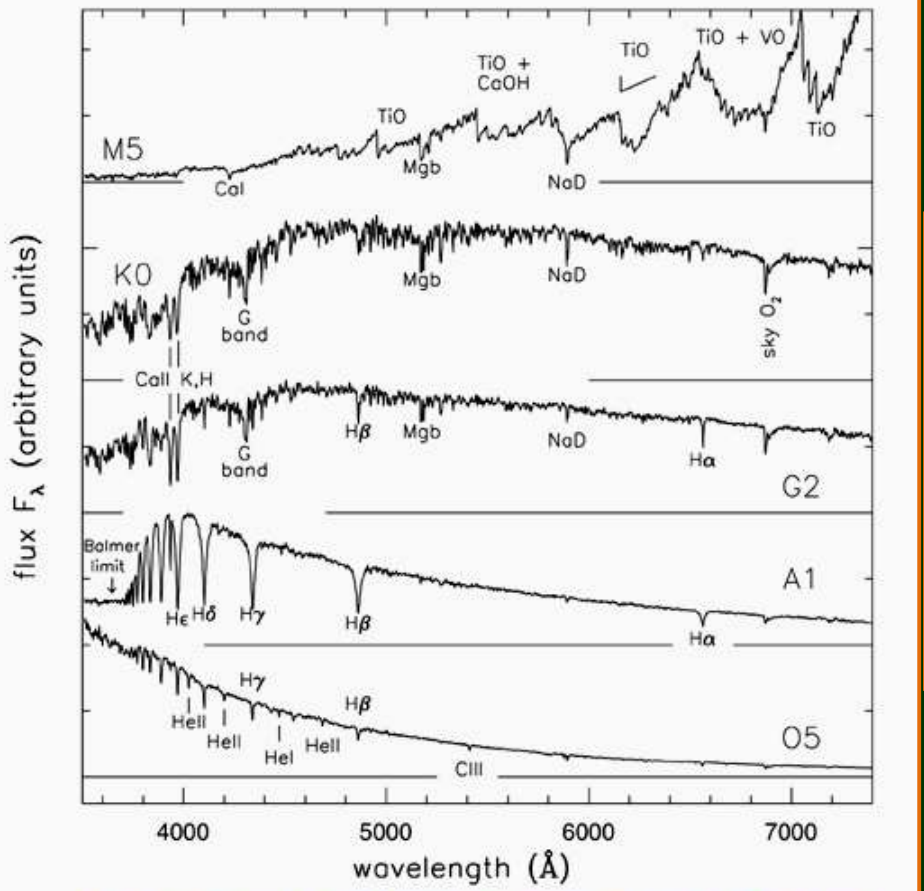

Fig 1.1 'Galaxies in the Universe' Sparke/Gallagher CUP 2007

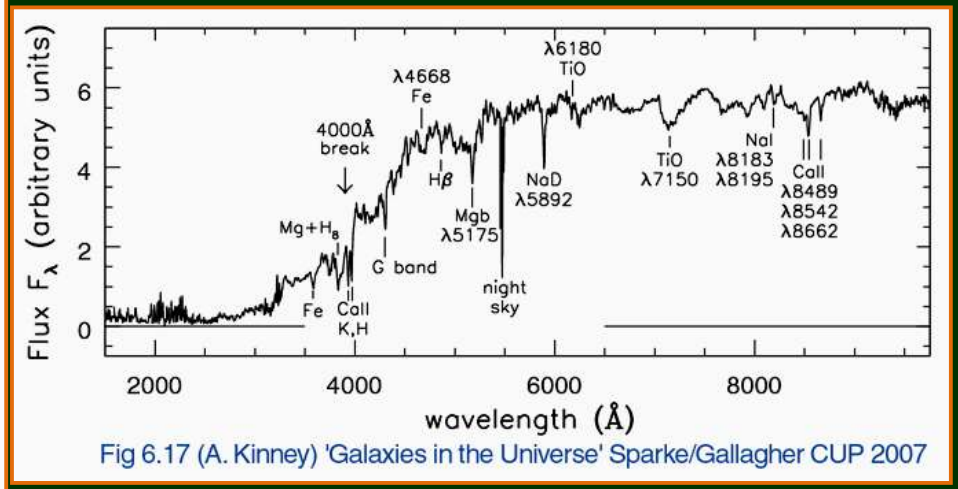

Fig 6.17 (A. Kinney) 'Galaxies in the Universe' Sparke/Gallagher CUP 2007

Comparación de espectros de galaxias lenticulares, espirales y con brotes de formación estelar

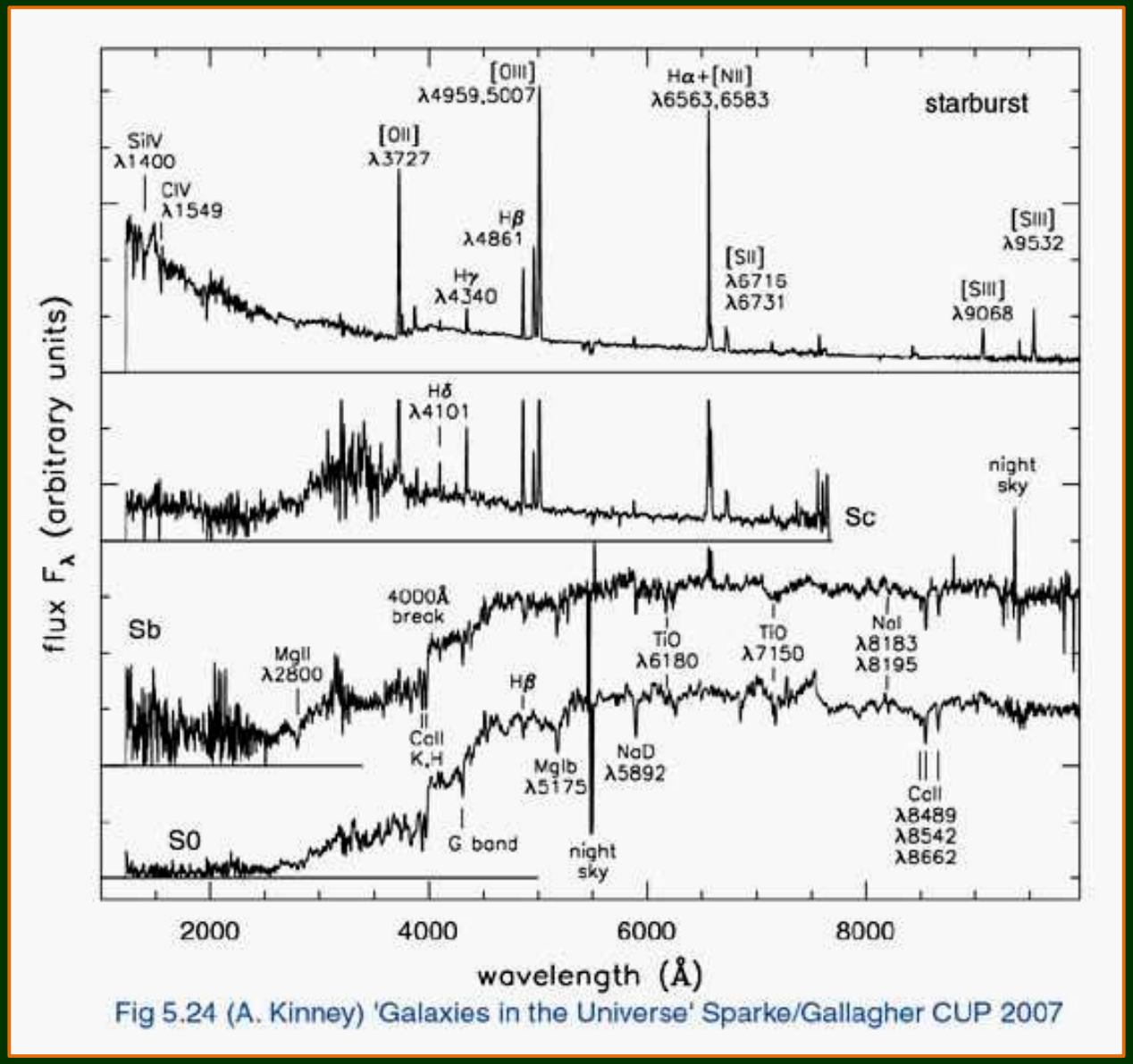

Fig 5.24 (A. Kinney) 'Galaxies in the Universe' Sparke/Gallagher CUP 2007

❖ Masa de galaxias espirales a partir de su curva de rotación

Ejemplo de líneas de un espectro de galaxia espiral

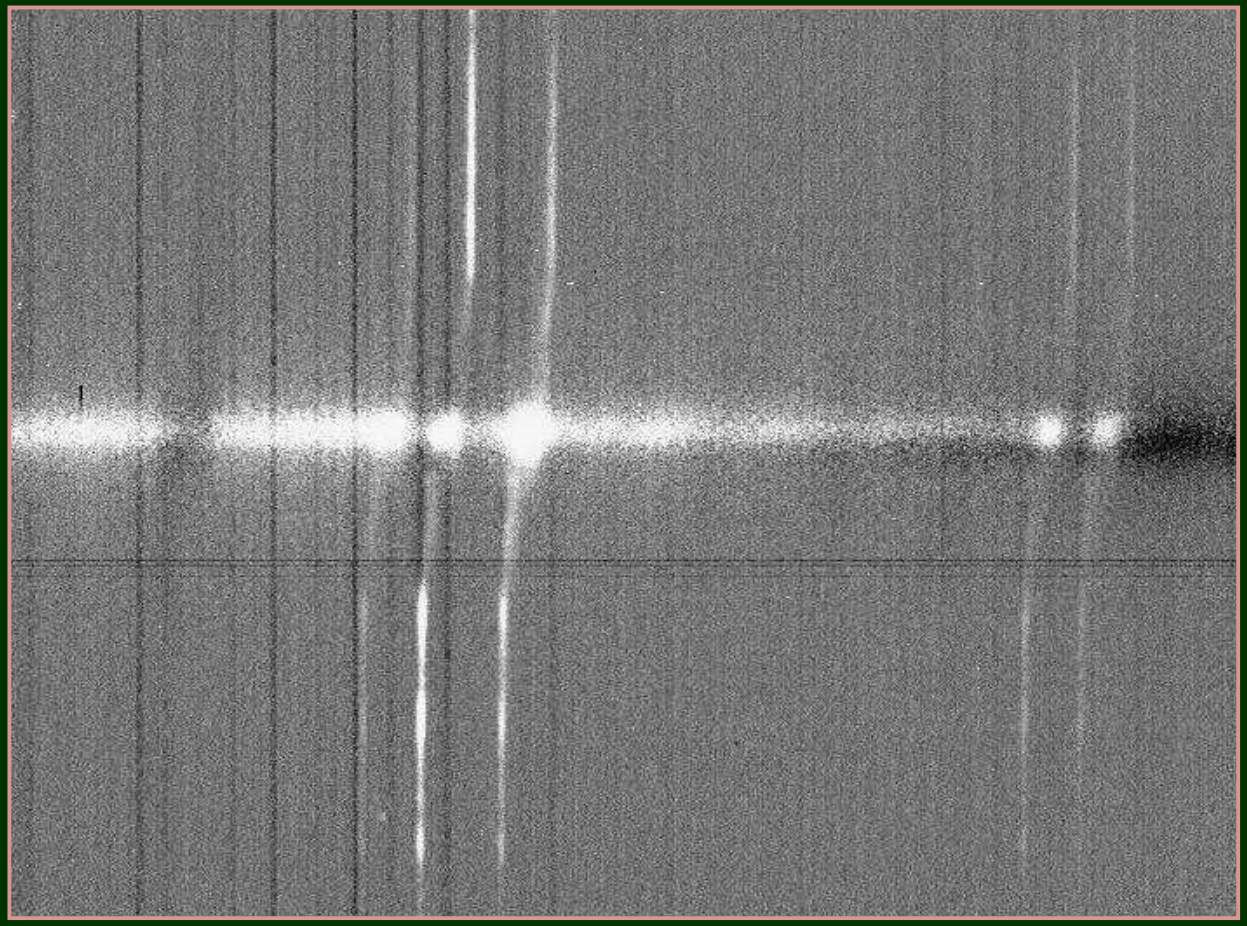

Ejemplo de líneas de un espectro de galaxia espiral

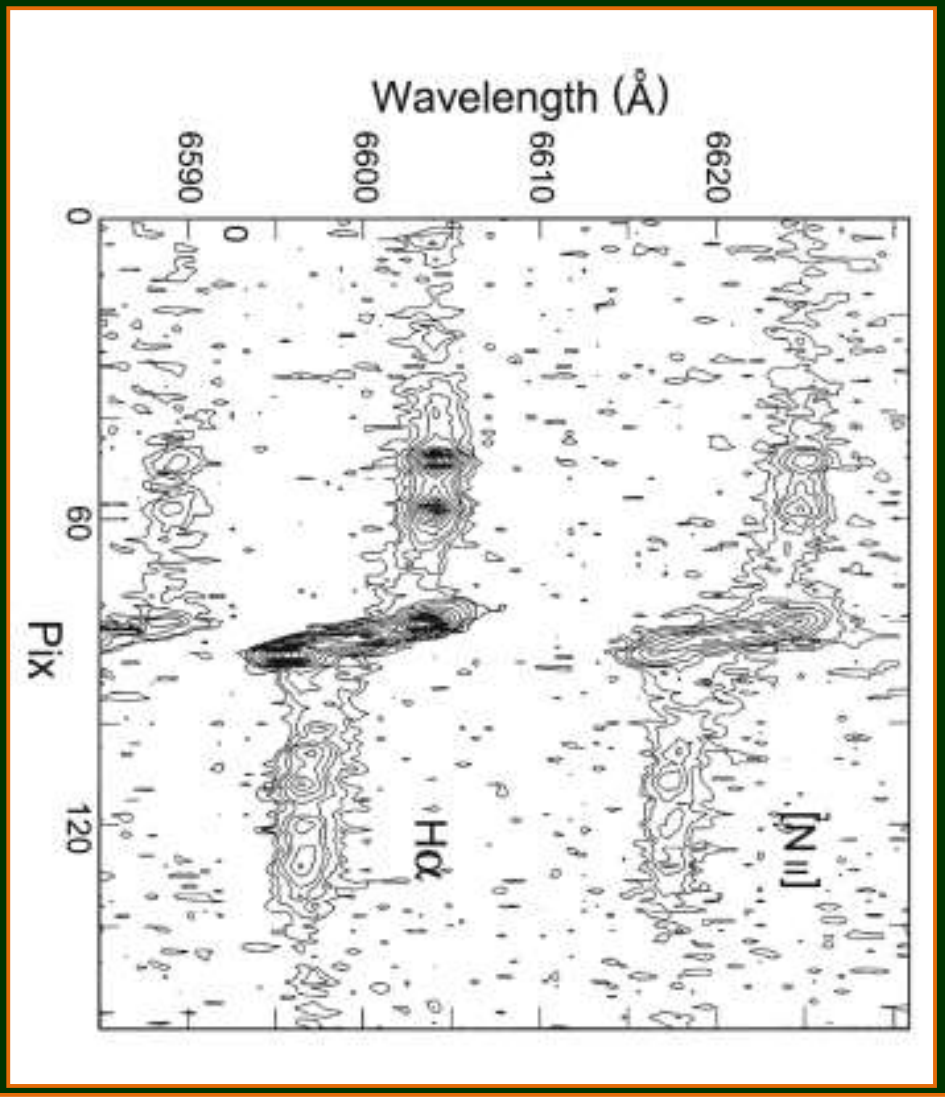

Fig. 9. Slit spectrum of the Hα 6563 Å and [N II] 6584 Å lines along the major axis of Sb galaxy NGC 4527 (Sofue et al. 1999).

Sofue et al. 1999, PASJ 51, 737

Curvas de rotación de galaxias espirales y enanas

Curvas de rotación

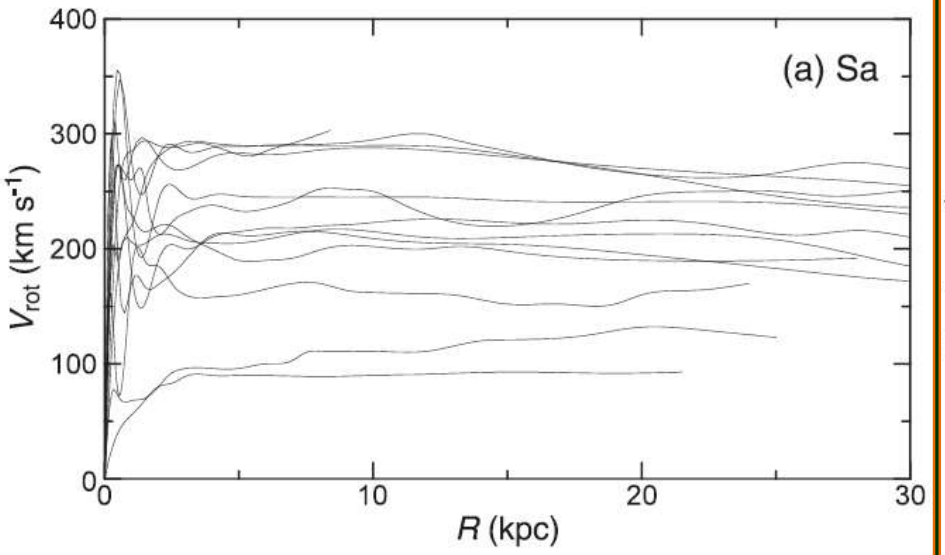

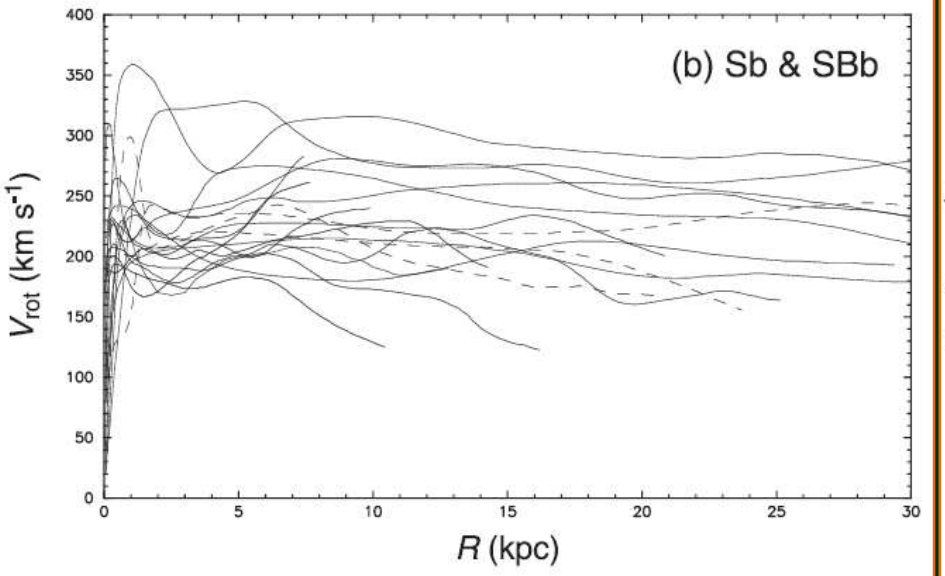

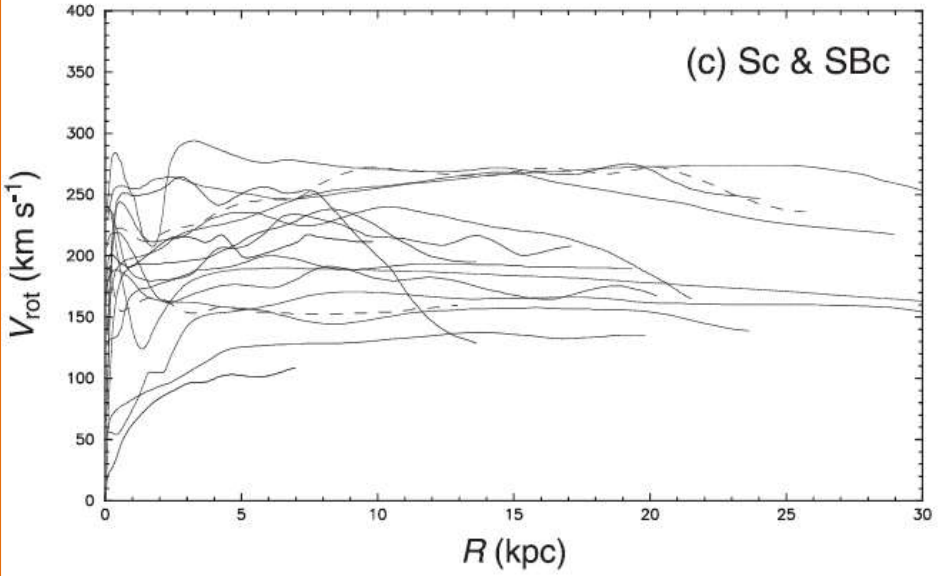

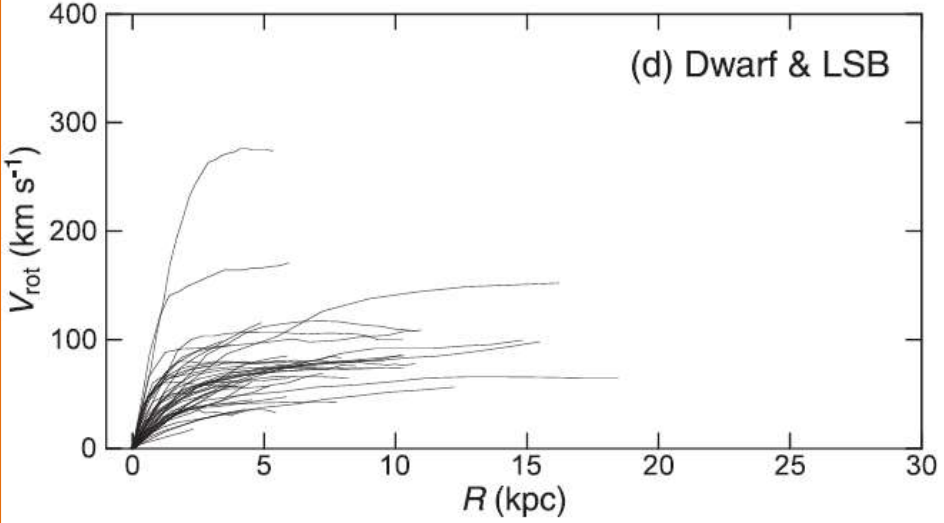

Sofue 2017, PASJ 69, R1

Determinación de la curva de rotación: caso general

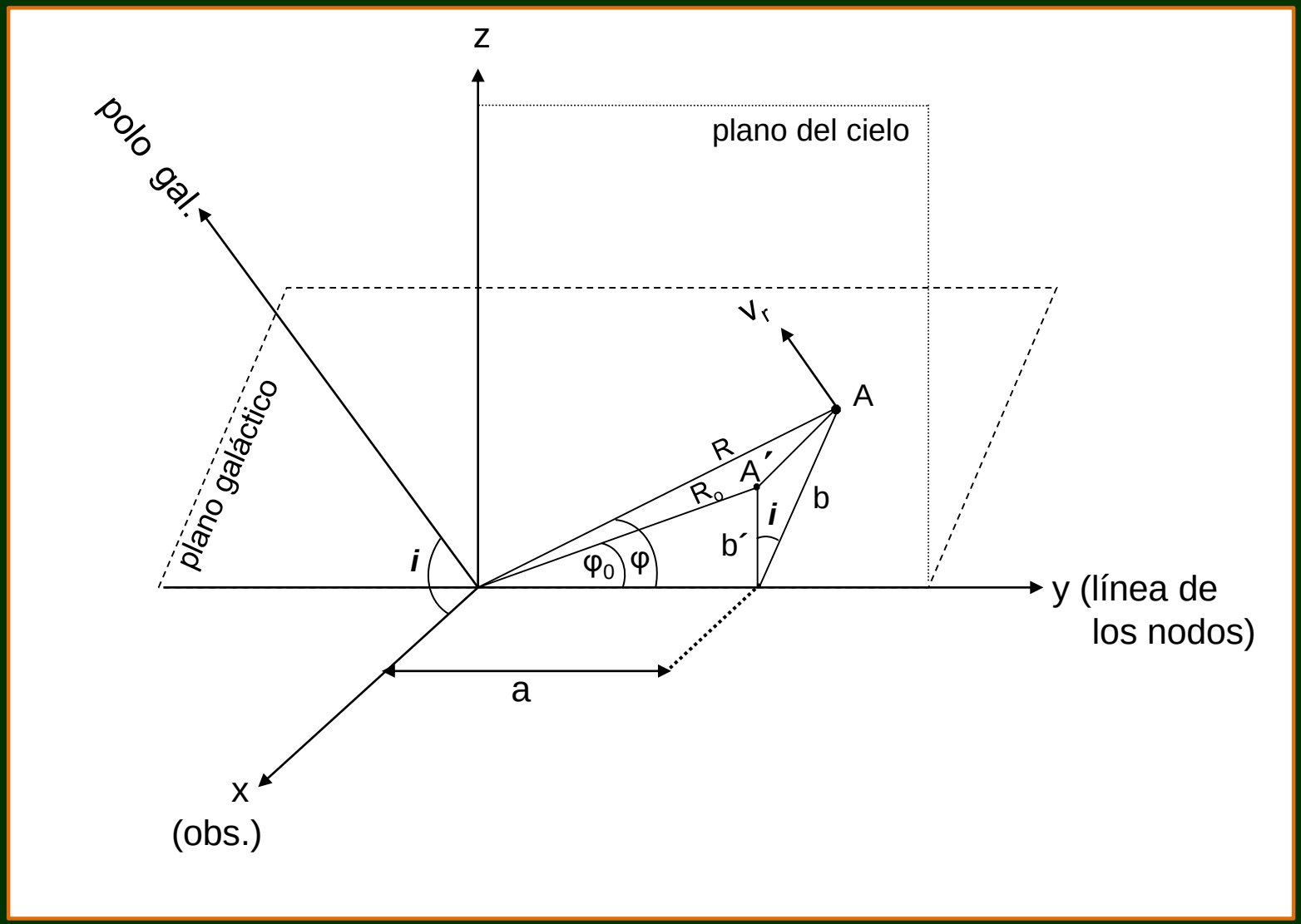

Curva de rotación de la Vía Láctea

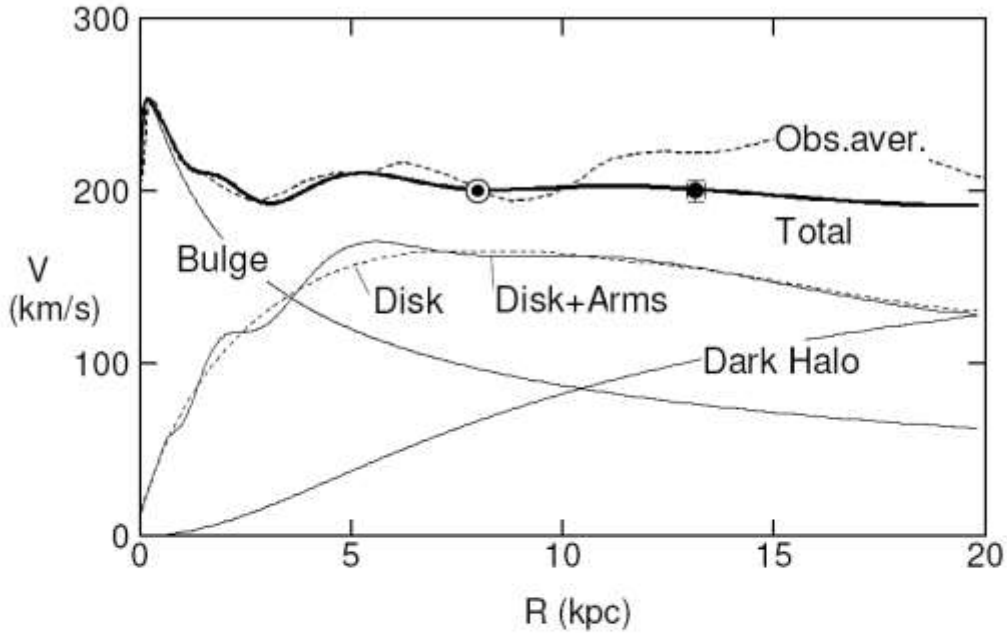

Fig. 3. Composite rotation curve including the bulge, disk, spiral arms, and dark halo. The big dot denotes the observed result from VERA (Honma et al. 2007). The pure disk component is also indicated by the thin dashed line. The thick dashed line indicates a simply averaged observed rotation curve taken from Sofue et al. (1999) where the outer curve is based only on the HI data of Honma and Sofue (1997a).

Sofue et al. 2009, PASJ 61, 227

Curvas de rotación analíticas (a), densidad (b), y masa *M(R)* (c): bulbo + disco + halo de DM

(DM: materia oscura)

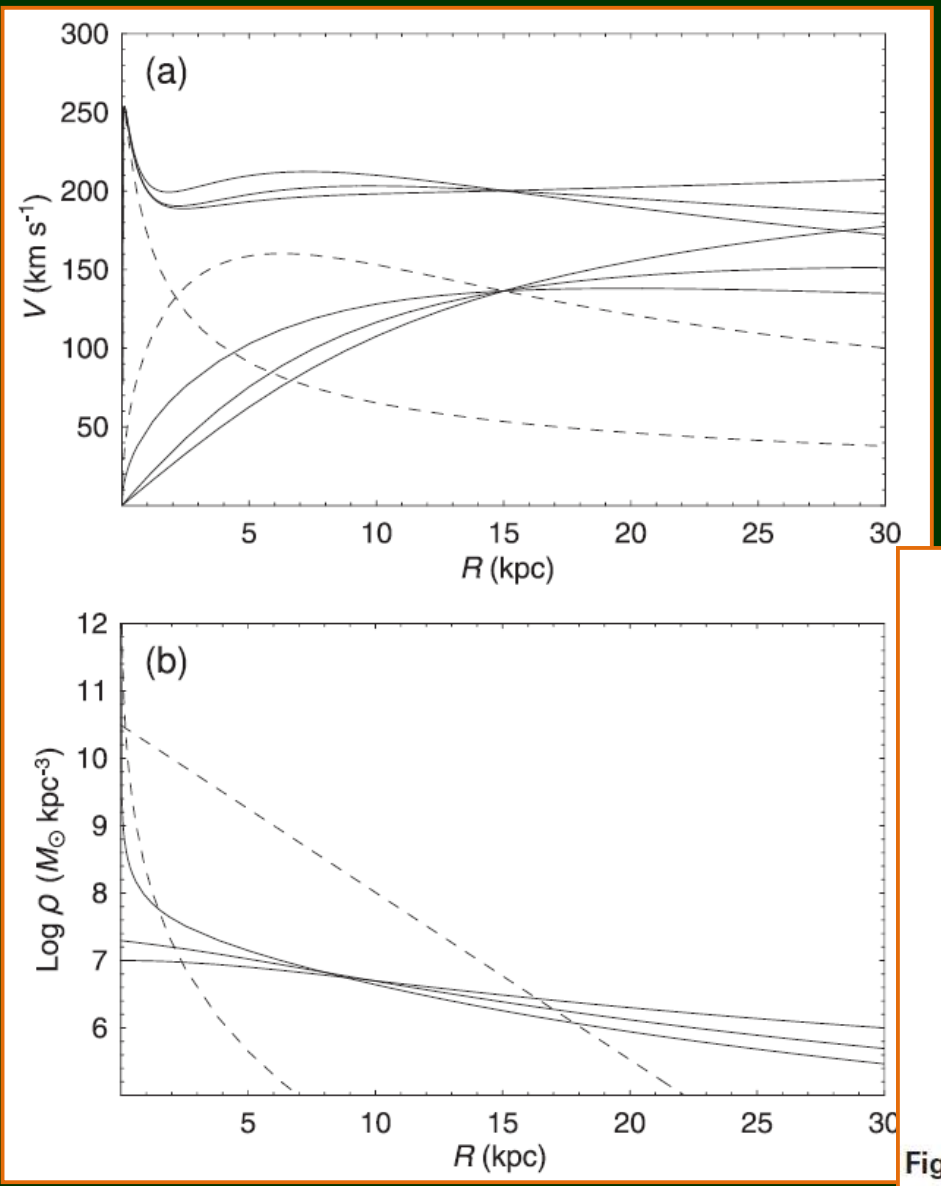

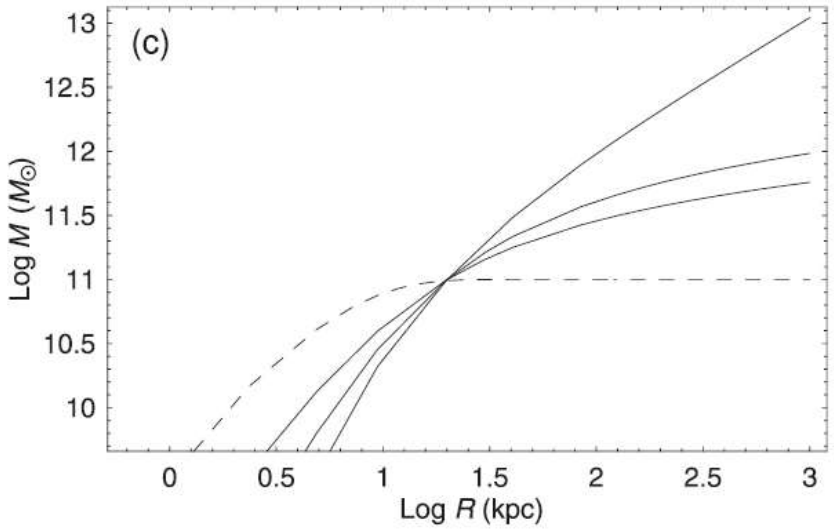

Fig. 25. (a) Analytic rotation curves composed of bulge, disk, and dark halo components represented by isothermal, Burkert (1995), and NFW models (upper solid lines from top to bottom at $R = 30$ kpc). Dashed lines represent the de Vaucouleurs bulge and exponential disks and three lower solid lines represent the halos as above. (b) Corresponding volume densities. (c) Corresponding enclosed mass within radius *r*.

Sofue 2017, PASJ 69, R1

Masa estelar
(bulbo+disco)

vs.

masa total
(bulbo+disco+DM)

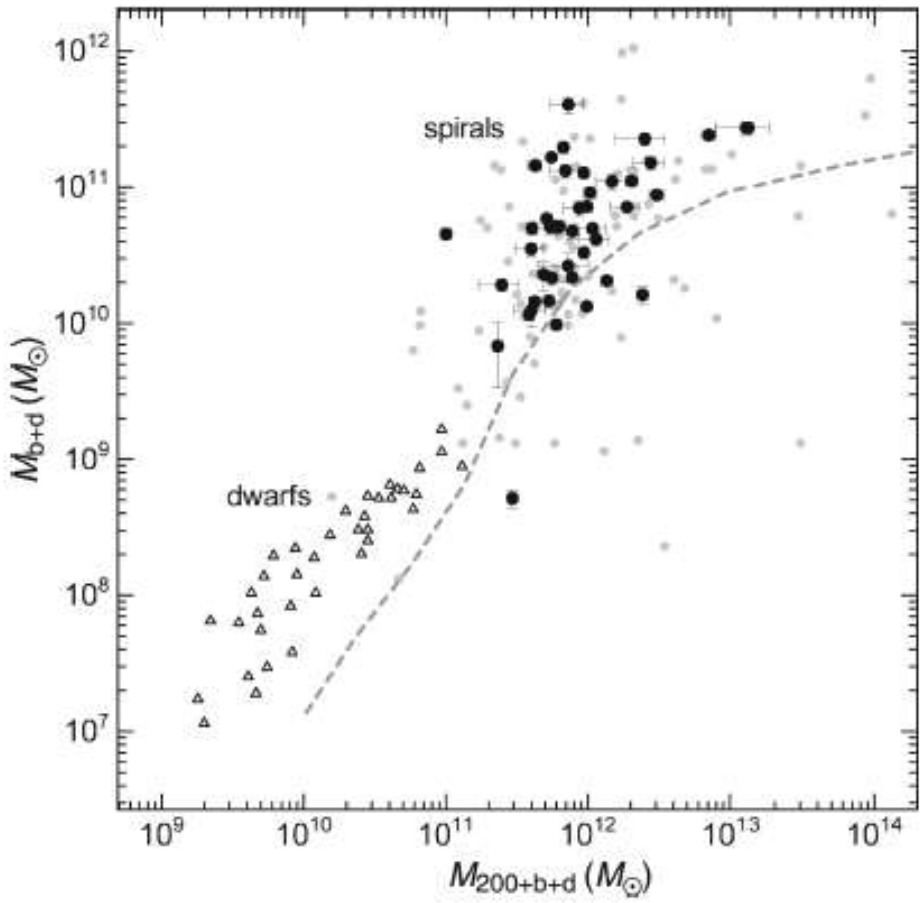

Fig. 33. M_{b+d}–$M_{200+b+d}$ relation compared with the stellar mass–total mass relation for dwarf galaxies (triangles: Miller et al. 2014) and simulation + photometry (dashed gray line: Behroozi et al. 2013). Black dots are the selected galaxies with reasonable fitting results, while small gray dots as well as black dots show non-weighted results from automatic decomposition of all rotation curves.

Sofue 2017, PASJ 69, R1

❖ Masa de galaxias con halos de rayos-X

Imágenes X (Chandra) e imágenes ópticas (DSS) de M87 y NGC 1399

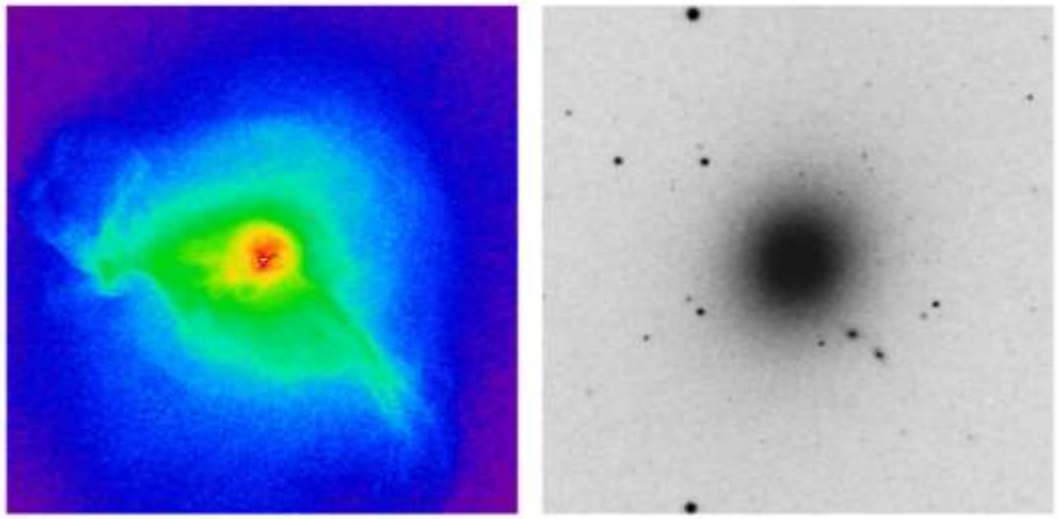

Figure 1. Central $10' \times 10'$ ($10' = 47$ kpc) region of the Chandra 0.6–2 keV (left) and DSS optical image (right) of M87. The galaxy appearance is very regular in the optical band, while the X-ray image is moderately disturbed. In these and other images throughout the paper, north is up and east is to the left.

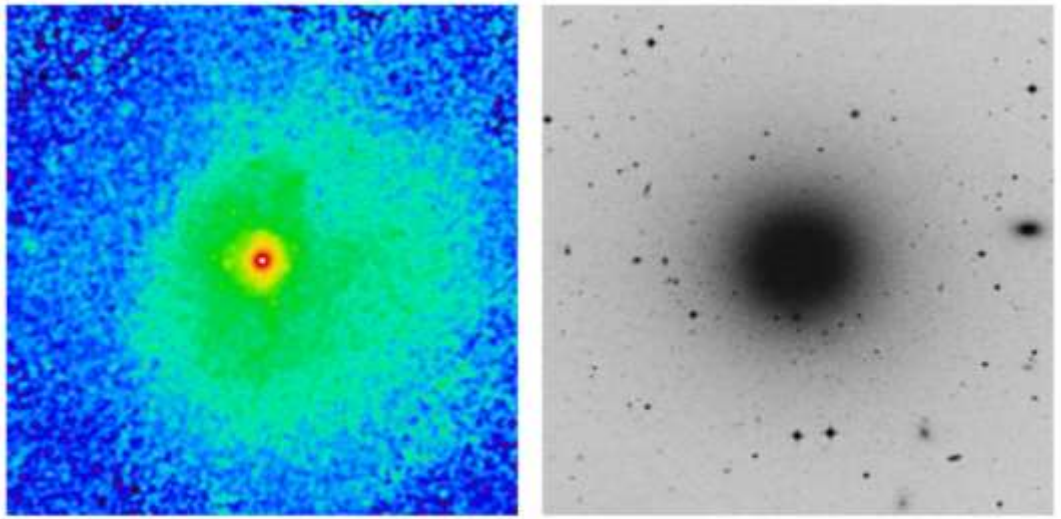

Figure 2. Central $10' \times 10'$ ($10' = 58$ kpc) region of the Chandra 0.6–2 keV (left) and DSS optical image (right) of NGC1399. As for M87, the optical galaxy is very regular, while the X-ray image shows only moderate deviations from spherical symmetry and appears considerably less disturbed than M87.

Churazov et al. 2008,
MNRAS 388, 1062

Mapa y perfil de brillo superficial X [0.2 a 4 KeV]

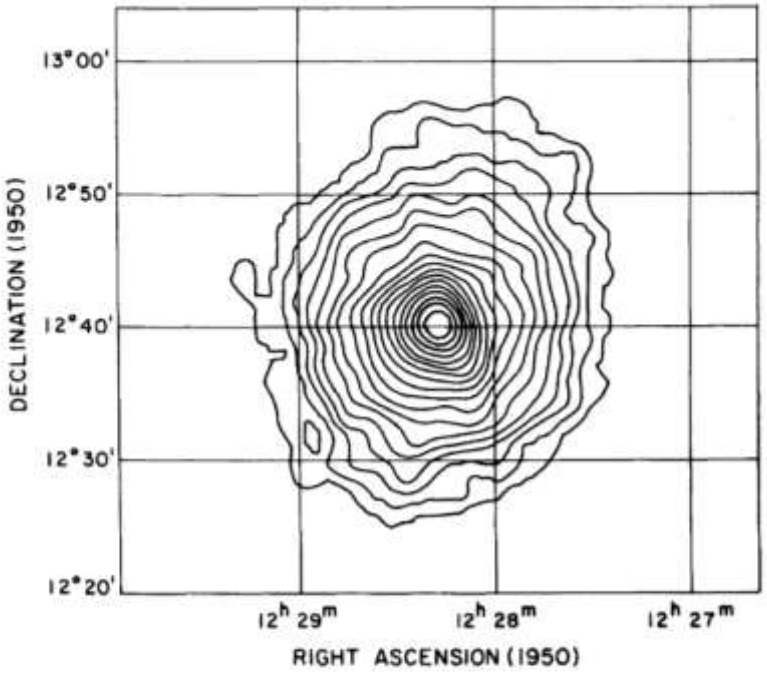

FIG. 2.—A 0.3–4.0 keV X-ray contour map made using data from the field centered on M87. Background has been subtracted, and a correction has been made for the vignetting of the telescope optics. The outermost contour is at a level of $\sim 1.9 \times 10^{-13}$ ergs cm^{-2} s^{-1} $arcmin^{-2}$, and the contour levels are separated by a factor of 1.2 in surface brightness. The data have been smoothed by convolution with a Gaussian function with $\sigma = 45''$. The outermost contour is slightly elliptical, with a ratio of major to minor axis of $\lesssim 1.2$. For an assumed distance to M87 of 15 Mpc, 1′ corresponds to 4.4 kpc.

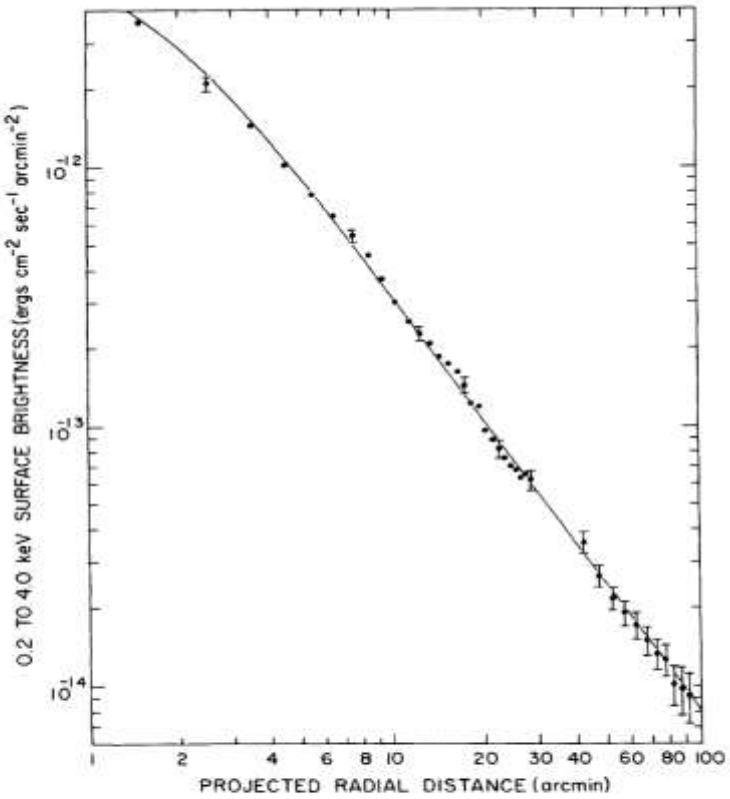

FIG. 3.—The 0.2–4.0 keV surface brightness profile of M87. Background has been subtracted, and a correction has been made for the vignetting of the telescope optics. The data within 30′ are from the field centered on M87. Beyond 30′, the average surface brightness of the four adjacent fields is shown. The curve indicates $S \propto [1 + (r/1.6)^2]^{-0.81}$. For a distance to M87 of 15 Mpc, 1′ corresponds to 4.4 kpc.

Fabricant et al. 1983, ApJ 267, 535

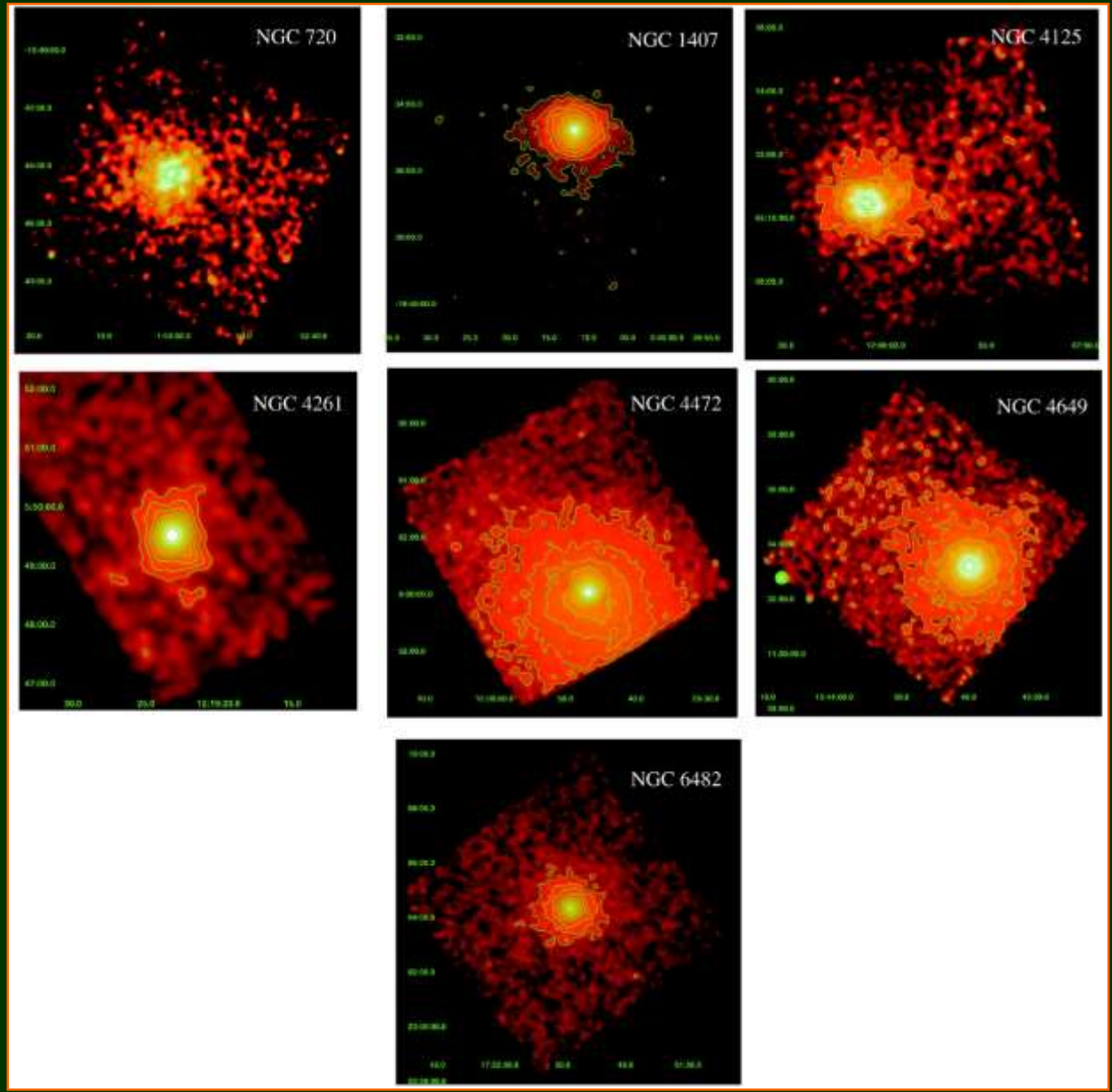

FIG. 1.—X-ray images of each of the galaxies in the sample. None of the systems show evidence of large-amplitude disturbances, which would indicate a violation of hydrostatic equilibrium. Some lower amplitude asymmetries do persist in some of the images, which we discuss in detail in § 7.4.

Imágenes X (Chandra) de galaxias E

Humphrey et al. 2006, ApJ 646, 899

Perfiles de T y de brillo superficial X [0.5 a 1.5 KeV] de NGC 1399 y NGC 3923

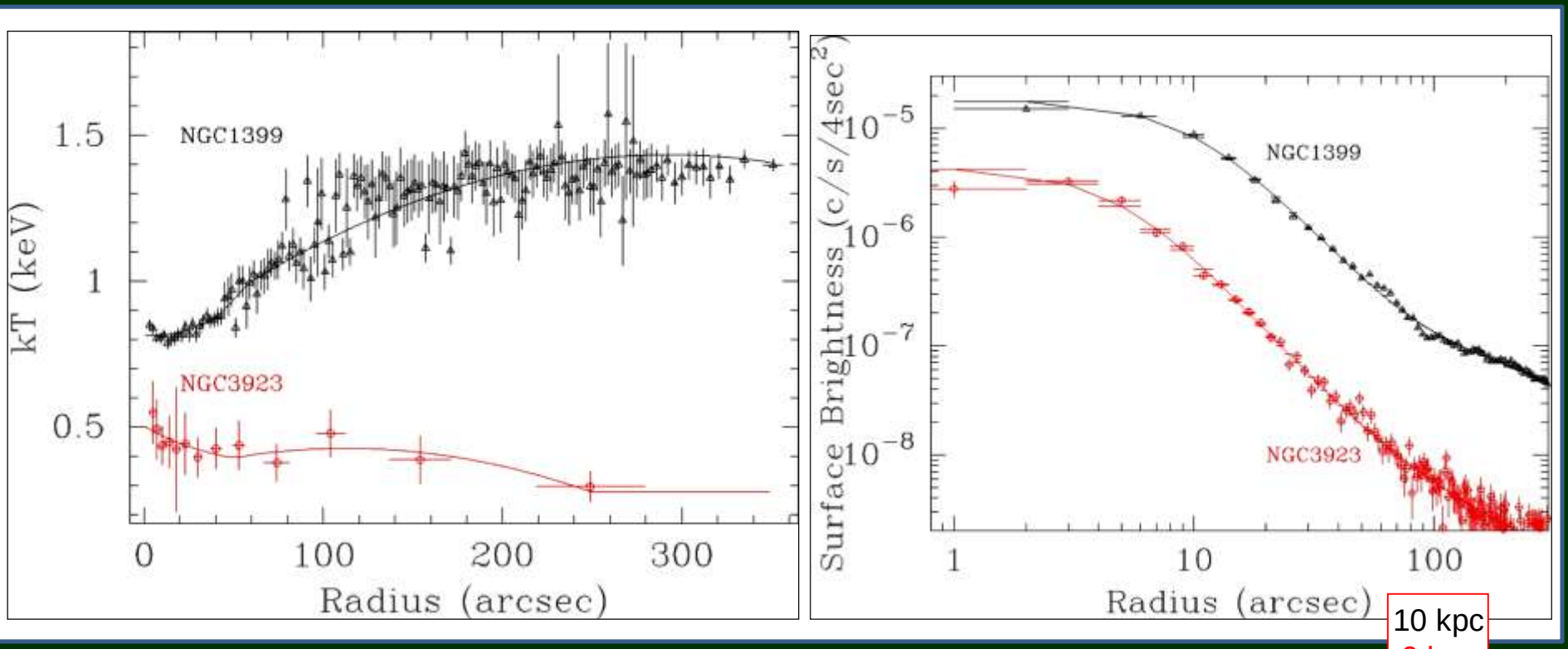

Fukazawa et al. 2006, ApJ 636, 698

Perfiles de masa de galaxias E

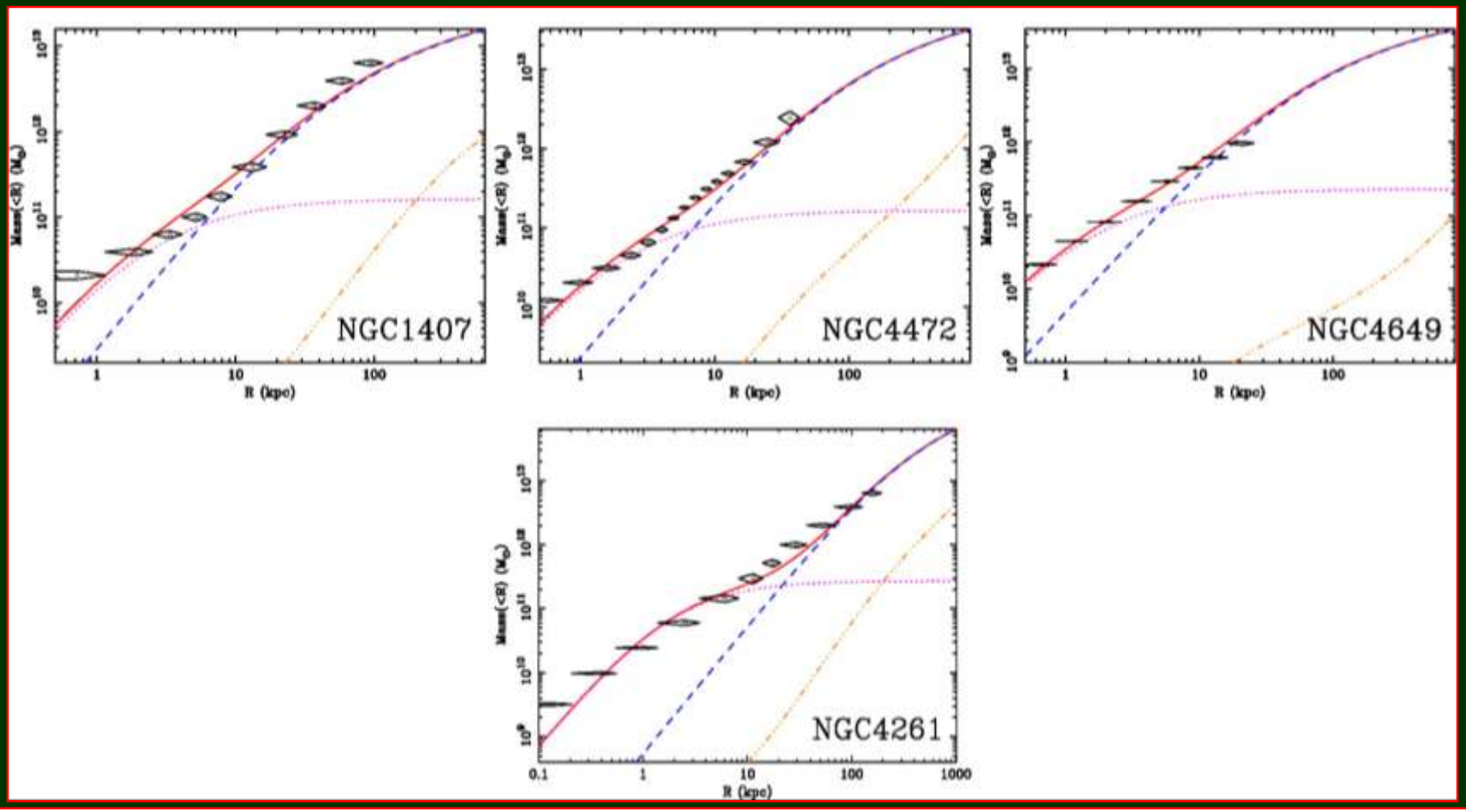

FIG. 6.—Mass profiles for each galaxy. The data points were computed using parameterized profile modeling (§ 6.4). In addition we show the best-fit NFW+stars mass models from assumed potential modeling, which generally agree reasonably well with the data points, indicating the consistency of both approaches to determine the mass profiles. We show the total gravitating mass model (*solid line*) and, separately, the stellar mass contribution (*dotted line*), the DM contribution (*dashed line*), and the gas mass (*dash-dot-dot-dot line*). The models are extrapolated out to R_{vir}. Errors shown are 1 σ.

Humphrey et al. 2006